

COVER PAGE

Document downloaded by @DAEL

Fri Nov 27 00:52:03 2026
For personal use

When automatic English translation is provided, only the original document is authentic.
The EAA cannot be held responsible of any translation error

Bibliographical reference

Multistatic Sonar Imaging: Comparisons Between the Matched Filtering Method and a Reconstruction Method Based on the Kirchhoff Approximation, Caroline Hervé, Jean-Pierre Sessarego, Régine Guillermin, Françoise Schmitt and Franck Daout, Acta Acustica **vol. 96** (Number 1), 2010, pp. 49-62

DOI
https://doi.org/10.3813/AAA.918255

Acta Acustica united with Acustica
Vol. 96 (2010) 49 – 62

DOI 10.3813/AAA.918255

Multistatic Sonar Imaging: Comparisons Between the Matched Filtering Method and a Reconstruction Method Based on the Kirchhoff Approximation

Caroline Hervé[1)], Jean-Pierre Sessarego[1)], Régine Guillermin[1)], Françoise Schmitt[2)], Franck Daout[2)]
[1)] CNRS UPR-7051, Laboratoire de Mécanique et d'Acoustique, 13402 Marseille, France.
herve@lma.cnrs-mrs.fr
[2)] SATIE UMR-8029, ENS Cachan, France.

Summary
In this study, comparisons are made between two imaging techniques in the context of the Multistatic Synthetic Aperture Sonar (SAS): the Matched Filtering method and a reconstruction method based on the Kirchhoff Approximation (KA). The Matched Filtering Algorithm (MFA) is the classical method used for image formation purposes in synthetic aperture systems. In this method the field diffracted by the target is approached by the "point scatterers" model. One of the first objective of this work is to develop a more complex and more realistic model than the well known "point scatterers" model. In addition, the aim is to get not only the shape and the size of target but also some quantitative information about its physical properties. Thus, a forward model based on the KA is proposed to get a more realistic description of the scattered field and a reconstruction method has been obtained through the use of a 2-D Fourier transform of this forward model. The algorithm hence obtained is named: "Imaging Reconstruction Algorithm in the Kirchhoff Approximation" (IRAKA). In this paper the IRAKA is compared to the MFA in order to check its capability to reconstruct target shape.
Images of 2-D targets of circular and elliptic cross-sections are reconstructed with the MFA and with the IRAKA from both numerical data and tank experimental data. These imaging methods are compared in terms of quality of the shape reconstruction and in terms of their robustness to noise in a given multistatic configuration. Both algorithms are also used to reconstruct images of a 2-D target of circular cross-section in a multistatic forward looking SAS context. With a good Signal to Noise Ratio (SNR) we get better results with the IRAKA than with the MFA in terms of the quality of target shape reconstruction. In presence of additive white Gaussian circular noise, the MFA off course, gives better results than the IRAKA. Nevertheless, using a technique of stabilization of the deconvolution, it has been possible to improve the performances of the IRAKA even in presence of additive noise.

PACS no. 43.30.-k, 43.30.Gv, 43.30.Vh, 43.30.Wi

1. Introduction

Monostatic Synthetic Aperture Radar or Sonar (SAR or SAS) systems are high resolution systems used for target imaging purposes which are now commonly used in radar and underwater acoustics applications [1, 2]. Bistatic SAR is operational in the radar domain [3] but few theoretical or experimental studies have been published on this subject in the underwater acoustics domain [4]. Multistatic SAS is currently under active consideration for use in applications such as detection and identification of buried mines, mines lying on the seabed or diver detection for harbour protection purposes. In the monostatic configuration, the transmitter and the receiver are located on the same carrier, whereas they are separated in the bistatic configuration. In a multistatic context, combination of various bistatic measurements allows to obtain different information than in a monostatic context as the scene is observed under more various angles. Another interesting feature of multistatic configuration is that it allows to choose transducer locations, which makes this kind of configuration capable of meeting all possible experimental constraints.

Here, it is proposed to make comparisons between two different imaging methods based on two different models of the scattered field: the Matched Filtering method and a reconstruction method based on the Kirchhoff Approximation (KA) of the scattered field. This study is performed in 2-D to simplify the problem, but the conclusions reached are not restrictive to 2-D situations. To meet the 2-D hypothesis, transducers are all placed in the plan (xOy) and

Received 20 May 2008,
accepted 30 September 2009.

© S. Hirzel Verlag · EAA

targets are supposed to be infinite in the (Oz) direction (2-D targets).

The SAR and SAS imaging techniques are based on signal theory [5, 6]. Most imaging reconstruction algorithms are issued from the Matched Filtering Algorithm (MFA) [7, 8]. In the MFA, the model used to estimate the diffracted field is the "point scatterers" model. It means that the target can be considered as a sum of "point scatterers" where the "point scatterer" is defined as a point that scatters waves with the same amplitude in any direction for any frequency. The received signal is then the sum of all the signals coming from all point scatterers (each elementary signal being a delayed copy of the transmitted signal with an amplitude attenuation). This model has shown its efficiency in the monostatic case.

One of the first objective of this work is to develop a more complex and more realistic model than the well known "point scatterers" model in a multistatic context. In addition, the aim is to get not only the shape and the size of target but also some quantitative information about its physical properties. Thus, the model of the received signal proposed here is based on a Boundary Integral Equation Method (BIEM) and the KA. A 2-D Fourier transform is then performed to invert the forward model and so to develop the imaging algorithm called IRAKA. The application of a 2-D stationary phase method to this 2-D Fourier transform yields a function reaching a maximum value on the target boundary. This reconstruction technique has been previously used for the case of a perfectly reflecting target for nondestructive testing of materials and for geophysical applications [9, 10]. Here it is adapted to the case of an elastic target in a multistatic context. The IRAKA has been developped by assuming that the propagation medium is homogeneous i.e. without sound speed variation. To take into account a speed variation in the IRAKA, it would be necessary to introduce this variation in the equation of propagation and then, in the integral expression of the acoustic field. In this work, we only focused on the capabilities of the IRAKA in the simplest case, but this method can be extended to more complex situations like buried objects detection and imaging.

First of all, the IRAKA has to be checked about its capability to reconstruct target shape. Comparisons are thus performed in terms of the quality of shape reconstruction. The criteria chosen to compare images reconstructed by each method are errors on target dimensions and thickness of target boundary. Detection limit is also evaluated for each method in presence of additive white gaussian noise. It is quantified by calculations of image entropy at different signal to noise ratios.

In the first part of this paper, geometrical and physical parameters are defined. In the second part, the MFA adapted to multistatic configurations is presented. In the third part, the reconstruction method based on the KA is presented and the IRAKA formula is derived. Then, in the fourth part, images of 2-D targets of circular and elliptic cross-sections are reconstructed by applying the MFA and the IRAKA to both numerical and tank experimental data.

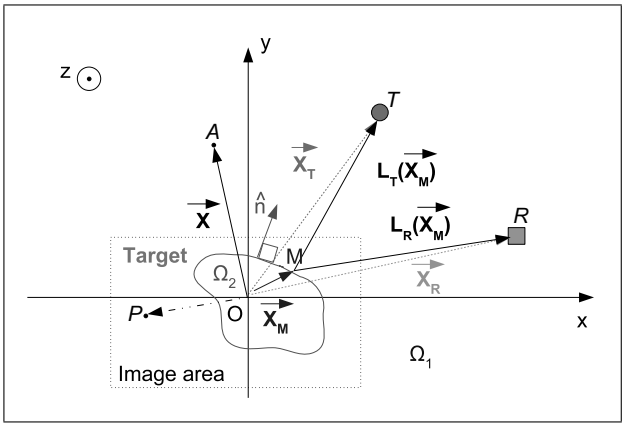


Figure 1. Bistatic configuration.

Then, images are compared in terms of their quality of target shape reconstruction and their robustness to additive white gaussian noise. Lastly, images of a 2-D target of circular cross-section are reconstructed with the MFA and the IRAKA in an experimental multistatic forward looking SAS context.

2. Geometrical and physical parameters

The aim of this study is to apply imaging methods to an immersed target insonified by several transducers used as transmitters. The waves diffracted by the target are recorded by several transducers used as receivers. This study is performed in 2-D geometry in order to reduce the computational time. (Oz) denotes the symmetry axis of the target. Transducers are placed in the plane (xOy). Figure 1 shows a bistatic configuration with a transmitter placed at T and a receiver placed at R.

The multistatic configuration is defined as a combination of several bistatic configurations. The 2-D target is arbitrarily placed in O in Figure 1.

The following vectors are defined:

- $\vec{X} = \vec{OA}$, where A is any point on the plane (xOy) and O is the geometrical center,
- $\vec{X_T} = \vec{OT}$, where T is the transmitter location,
- $\widehat{X_T} = \vec{X_T}/\|\vec{X_T}\|$ is the normalized vector of $\vec{X_T}$,
- $\vec{X_R} = \vec{OR}$, where R is the receiver location,
- $\widehat{X_R} = \vec{X_R}/\|\vec{X_R}\|$ is the normalized vector of $\vec{X_R}$,
- $\vec{X_M} = \vec{OM}$, where M is any point on the target boundary,
- $\hat{n}$ is the outgoing normal from the target boundary,
- $\vec{\xi} = \vec{OP}$, where P is one of the image pixels.

The following distances are defined:

- $L_T(\vec{X}) = \left\| \vec{X_T} - \vec{X} \right\|$,
- $L_R(\vec{X}) = \left\| \vec{X_R} - \vec{X} \right\|$.

The following angles with respect to the $(O\vec{x})$ axis are defined:

- $\widehat{(Ox, \vec{X_T})} = \theta_T$,
- $\widehat{(Ox, \vec{X_R})} = \theta_R$,

The target (denoted Ω_2) is immersed in water (free space, denoted Ω_1). Ω_1 and Ω_2 are assumed to be homogeneous and isotropic. ρ_1 is the water density and c_1 is the water sound speed. $k_1 = 2\pi f/c_1$ denotes the wavenumber in water, where f is the frequency. The targets are chosen convex, without corner nor roughness to avoid multiple diffraction that KA does not take into account. For simulations and experiments (parts 5 and 6), two target geometries are therefore chosen: a 2-D target of circular cross-section and an 2-D target of elliptic cross-section. These targets are made of stainless steel of density ρ_2, compression wave speed c_p and shear wave speed c_s. The half of the largest dimension of the targets (referred to below as a) is the radius of the 2-D target of circular cross-section. For the 2-D target of elliptic cross-section a is half of the large axis dimension.

3. Matched filtering reconstruction method

Matched Filtering is a well known imaging method in Synthetic Aperture Radar [7] and Sonar [8] domain. This method has been adapted to bistatic configurations in the case of SAR [7]. It is based on estimation theory and it is the most exact method in the sense of the maximum likelihood. A Matched filter is an optimum filter which maximises the signal to noise ratio in the presence of additive white gaussian circular noise. The signal received can then be written as

$$P^r(\vec{X}_R, k_1) = P^d(\vec{X}_R, k_1) + W(\vec{X}_R, k_1), \tag{1}$$

where $P^d(\vec{X}_R, k_1)$ is the field diffracted by the target at R and $W(\vec{X}_R, k_1)$ is the white circular Gaussian noise at R. For tank experimental data, the signal transmitted directly from the transmitter to the receiver is removed from data by time-filtering procedure. In this method, the diffracted field is modeled using the "point scatterers" model. It means that the target can be considered as a sum of N "point scatterers" where the "point scatterer" is defined as a point that scatters waves with the same amplitude in any direction for any frequency. σ_n denotes the reflexion coefficient of the "point scatterer" n located on the target boundary at point M_n. The target model is written

$$Target(\vec{\xi}) = \sum_{n=1}^{N} \sigma_n \, \delta(\vec{\xi} - \vec{X}_n) \tag{2}$$

The diffracted field by the target model is thus written

$$P^d(\vec{X}_R, k_1) = \sum_{n=1}^{N} \sigma_n \, P_0(f) \, \mathrm{e}^{-\mathrm{j}k_1 \left[L_T(\vec{X_{M_n}}) + L_R(\vec{X_{M_n}})\right]}, \tag{3}$$

where $\vec{X_{M_n}} = \vec{OM}_n$ and $P_0(f)$ denotes the transmitted signal spectrum.

The algorithm is first presented for one transmitter located at T and N_R receivers located at R_m. $I_M(\vec{\xi})$ is the complex amplitude of an image pixel located at P. It is the estimator of the maximum likehood of the reflexion coefficients σ_n based on measurements of $P^r(\vec{X}_R, k_1)$. The Matched Filtering method is performed on the full range of frequencies of the transmitted signal spectrum. Frequency values are discretized in N_f samples. The frequency sample is denoted: f_l, where $l = 1, N_f$, and the wavenumber sample is denoted: $k_{1_l} = 2\pi f_l/c_1$. The Matched Filtered Algorithm (MFA) formula for one transmitter and N_R receivers is written as [7]

$$I_M(\vec{\xi}) = \frac{\sum_{m=1}^{N_R} \sum_{l=1}^{N_f} P^r(\vec{X_{R_m}}, k_{1_l}) \, P_0^*(f_l) \, \mathrm{e}^{\mathrm{j}k_{1_l}\left[L_T(\vec{\xi}) + L_{R_m}(\vec{\xi})\right]}}{N_R \sum_{l=1}^{N_f} |P_0(f_l)|^2}, \tag{4}$$

where $P_0^*(f)$ is the conjugate of the transmitted signal spectrum.

Usually, "Matched Filtering" performs a 1-D processing and is called pulse compression but in SAR/SAS systems the MFA performs a 2-D operation. For each pixel of the image, the received signal is correlated to the replica pulse. This corresponds to the step of pulse compression. Then, a second correlation on receiver positions is performed. The MFA is implemented in frequency domain but it is also called "Time-Domain Correlation" when it is implemented in the time domain [6].

The image area is assumed to be far from the transmitter and receivers, thus

- $L_T(\vec{\xi}) = \|\vec{X}_T - \vec{\xi}\| \approx \|\vec{X}_T\| - \vec{\xi} \cdot \widehat{X_T}$,
- $L_{R_m}(\vec{\xi}) = \|\vec{X_{R_m}} - \vec{\xi}\| \approx \|\vec{X_{R_m}}\| - \vec{\xi} \cdot \widehat{X_{R_m}}$.

Hence the MFA can also be written as

$$I_M(\vec{\xi}) = \frac{\sum_{m=1}^{N_R} \sum_{l=1}^{N_f} \mathrm{e}^{\mathrm{j}k_{1_l}\left[\|\vec{X}_T\| + \|\vec{X_{R_m}}\|\right]} P^r(\vec{X_{R_m}}, k_{1_l}) \, P_0^*(f_l) \, \mathrm{e}^{-\mathrm{j}\vec{k_{l,m}}\vec{\xi}}}{N_R \sum_{l=1}^{N_f} |P_0(f_l)|^2}, \tag{5}$$

where $\vec{k_{l,m}} = k_{1_l}\left[\widehat{X_T} + \widehat{X_{R_m}}\right]$.

Equation (5) is used to reconstruct an image with one transmitter and several receivers. To obtain the multistatic image based on N_T transmitters, a coherent sum of these images is performed.

To obtain a multistatic image consisting of N_x by N_y pixels, the number of operations required by multistatic MFA will then be N_f by N_T by N_R by $(N_x\, N_y)$. The complexity will therefore be $O(N_f\, N_T\, N_R\, N_x\, N_y)$.

4. Kirchhoff reconstruction method

In the Matched Filtering reconstruction method, the "point scatterers" model is used to obtain the diffracted field expression. In this section an imaging method based on the KA is proposed. The approach to obtain this method can be summarised as

- Modeling of the scattered field:
  - The BIEM is used to obtain the field diffracted by a 2-D target with an arbitrary cross-section,
  - Then the KA also known as the tangent-plane method is applied to obtain the diffracted field P^d.

  In the expression of P^d, appears a function called v_d.
- Construction of the inversion algorithm:

– The 2-D Fourier Transform of v_d is calculated via a 2-D stationary phase method. It is found maximum on the target boundary,
– Finally, the last property is used to implement the imaging algorithm called the IRAKA. This algorithm is obtained by discretization of the expression of the 2-D Fourier Transform of v_d.

4.1. Modeling of the scattered field in the Kirchhoff Approximation

In what follows, the temporal dependance is chosen such as $e^{+j\omega t}$.

Let $P(\vec{X}, k_1)$ be the total field at a point A on the plane (xOy) where the coordinate vector is $\vec{X}$. $\forall \vec{X_R}, \vec{X_M} \in R^2$, the free-space Green function is denoted $G(\vec{X_R}, \vec{X_M})$.

The diffracted field at point R is written

$$P^d(\vec{X_R}, k_1) = \int_{\Gamma_{12}} \left\{ P(\vec{X_M}, k_1)\, \hat{n}\cdot\vec{\text{grad}} G(\vec{X_R}, \vec{X_M}) - G(\vec{X_R}, \vec{X_M})\, \hat{n}\cdot\vec{\text{grad}} P(\vec{X_M}, k_1) \right\} d\Gamma(\vec{X_M}), \quad (6)$$

where Γ_{12} is the target boundary.

Since this study is performed in 2-D, the incident wave is modeled in the form of a cylindrical wave propagating in Ω_1. The incident field is therefore written

$$P^t(\vec{X_M}, k_1) = -\frac{j}{4} H_0^2 \left[k_1 L_T(\vec{X_M})\right] P_0(f), \quad (7)$$

where H_0^2 is the Hankel function of the second kind and of order 0.

Under Physical Optics assumption, the insonified part of the target (referred to below as Γ_{12e}) is the only part of the target involved in the expression of the diffracted field. Thus, the field diffracted by the part of the target which is located in the shadow is considered equal to zero.

KA is then applied. This method has been used by many authors [11, 12, 13, 14, 15] for modeling rough surface diffraction. KA does not take into account multiple reflexion thus targets are chosen convex without edge nor roughness. KA is a high frequency approximation thus $k_1 a$ must be greater than 1. At each point M on Γ_{12e}, the elastic reflexion coefficient is denoted $R_c(\vec{X_M})$. Applying KA, (6) can be written as

$$P^d(\vec{X_R}, k_1) = \int_{\Gamma_{12e}} R_c(\vec{X_M}) \left[P^t(\vec{X_M}, k_1) \frac{\partial G(\vec{X_R}, \vec{X_M})}{\partial n} + G(\vec{X_R}, \vec{X_M}) \frac{\partial P^t(\vec{X_M}, k_1)}{\partial n} \right] d\Gamma(\vec{X_M}). \quad (8)$$

The 2-D free-space Green function is

$$G(\vec{X_R}, \vec{X_M}) = -\frac{j}{4} H_0^2 \left[k_1 L_R(\vec{X_M})\right]. \quad (9)$$

The far field approximations $k_1 L_R(\vec{X_M}) \gg 1$ and $k_1 L_T(\vec{X_M}) \gg 1$ are applied to perform the asymptotic developement of the Hankel function of the second kind [16]. In addition, the target boundary is assumed to be located far from transmitters and receivers.

Given previous approximations, the following model is obtained for the diffracted field

$$P^d(\vec{X_R}, k_1) = \frac{e^{-jk_1(\|\vec{X_T}\|+\|\vec{X_R}\|)} P_0(f)}{8\pi\sqrt{\|\vec{X_T}\|\|\vec{X_R}\|}} \cdot v^d\left(\widehat{X_T} + \widehat{X_R}, k_1\right), \quad (10)$$

where

$$v^d(\widehat{X_T} + \widehat{X_R}, k_1) = \int_{\Gamma_{12e}} R_c(\vec{X_M})\left(\widehat{X_T} + \widehat{X_R}\right) \cdot \hat{n}\, e^{+jk_1\left(\widehat{X_T}+\widehat{X_R}\right)\cdot\vec{X_M}}\, d\Gamma(\vec{X_M}). \quad (11)$$

Comparing the diffracted field based on "point scatterers" model (3) with the diffracted field based on the KA (10), it can be observed that σ_n, becomes $R_c(\vec{X_M})(\widehat{X_T} + \widehat{X_R})$ in the diffracted field based on the KA. There is a geometrical factor $(\widehat{X_T} + \widehat{X_R})\cdot\hat{n}$ that is absent in the "point scatterers" model. In the bistatic case, the diffracted field based on the KA is thus more comprehensive than the diffracted field based on the"point scatterers" model.

In (10), as $(\widehat{X_T}+\widehat{X_R}) = \vec{0}$ involves $v^d(\widehat{X_T}+\widehat{X_R}, k_1) = 0$, no measurements will therefore be made in the transmission mode in this study.

4.2. Construction of the inversion algorithm IRAKA

The following study carried out the case where one transmitter is located at T and where there are several receivers. The 2-D Fourier transform of $v^d(\widehat{X_T} + \widehat{X_R}, k_1)$, defined in (11), is written as

$$f(\vec{\xi}) = \int_{k_x}\int_{k_y} v^d\left(\widehat{X_T} + \widehat{X_R}, k_1\right) e^{-j\vec{k}\cdot\vec{\xi}}\, dk_y\, dk_x. \quad (12)$$

The coordinate system is then changed from (k_x, k_y) to (k_1, θ_R), so that $\vec{k} = k_x\hat{x}+k_y\hat{y} = k_1(\widehat{X_T}+\widehat{X_R})$. Hence, $\vec{k} = k_1[\cos\theta_T + \cos\theta_R]\hat{x} + k_1[\sin\theta_T + \sin\theta_R]\hat{y}$. The Jacobian is therefore written as follows: $J = k_1\,[1+\cos(\theta_T - \theta_R)]$. $f(\vec{\xi})$ becomes

$$f(\vec{\xi}) = \int_{-\infty}^{\infty}\int_{0}^{2\pi} k_1\left[1 + \cos(\theta_T - \theta_R)\right] \cdot v^d\left(\widehat{X_T} + \widehat{X_R}, k_1\right) e^{-j\vec{k}\vec{\xi}}\, d\theta_R\, dk_1. \quad (13)$$

Usually, the reception angle range and the frequency range are both limited. Reception angles θ_R range between $\theta_{R_{min}}$ and $\theta_{R_{max}}$. Hence, $\Delta\theta_R = \theta_{R_{max}} - \theta_{R_{min}}$ denotes the reception angle range. $k_0 = 2\pi f_0/c_1$ denotes the wavenumber linked to the central frequency of the transmitted signal f_0 and $\Delta k = 2\pi B/c_1$ denotes the wavenumber range linked to the bandwith B of the transmitted signal. The integration domain will therefore be limited using the function: $F(\theta_R, k_1) = 1$ if $(k_0 - \Delta k/2) \le k_1 \le (k_0 + \Delta k/2)$ and $\theta_{R_{min}} \le \theta_R \le \theta_{R_{max}}$. $F(\theta_R, k_1) = 0$ otherwise. Then, $\tilde{v^d}(\widehat{X_T} + \widehat{X_R}, k_1)$ is defined as $\tilde{v^d}(\widehat{X_T} + \widehat{X_R}, k_1) =$

$F(\theta_R, k_1)\, v^d(\widehat{X_T} + \widehat{X_R}, k_1)$. Therefore,

$$\tilde{f}(\vec{\xi}) = \int_{k_0-\frac{\Delta k}{2}}^{k_0+\frac{\Delta k}{2}} \int_{\theta_{R_{min}}}^{\theta_{R_{max}}} k_1 \left[1+\cos(\theta_T-\theta_R)\right] \cdot \tilde{v}^d(\widehat{X_T}+\widehat{X_R}, k_1)\, \mathrm{e}^{-\mathrm{j}\vec{k}\cdot\vec{\xi}}\, \mathrm{d}\theta_R\, \mathrm{d}k_1. \quad (14)$$

Hence,

$$\tilde{f}(\vec{\xi}) = \int_{k_0-\frac{\Delta k}{2}}^{k_0+\frac{\Delta k}{2}} k_1\, \Phi(\vec{\xi}, k_1)\, \mathrm{d}k_1, \quad (15)$$

with

$$\Phi(\vec{\xi}, k_1) = \int_{\theta_{R_{min}}}^{\theta_{R_{max}}} \int_{\Gamma_{12e}} g(\theta_R, \vec{X_M}) \cdot \mathrm{e}^{+\mathrm{j}k_1 h(\theta_R, \vec{X_M})}\, \mathrm{d}\Gamma(\vec{X_M})\, \mathrm{d}\theta_R, \quad (16)$$

where

$$g(\theta_R, \vec{X_M}) = \left[1+\cos(\theta_T-\theta_R)\right] R_c(\vec{X_M}) \cdot \left(\widehat{X_T}+\widehat{X_R}\right)\cdot\hat{n}, \quad (17)$$

and where

$$h(\theta_R, \vec{X_M}) = \left(\widehat{X_T}+\widehat{X_R}\right)\cdot\left(\vec{X_M}-\vec{\xi}\right). \quad (18)$$

When the phase term of integral (16) oscillates more rapidly than the function $g(\theta_R, \vec{X_M})$, the stationary phase method gives an approximated value of the integral Φ [17]. This method consists first in finding stationary points. These points can be obtained from the stationary conditions

$$\begin{cases} \partial h/\partial\Gamma(\vec{X_M}) = 0, \\ \partial h/\partial\theta_R = 0, \end{cases}$$

where $\Gamma(\vec{X_M})$ is the curvilinear abscissa at point M.

The previous 2-D stationary conditions give a condition on point M of the target boundary and reception angle θ_R. The solution is denoted by the couple $(\theta_{R_{SP}}, \vec{X_{M_{SP}}})$. The normalized vector of $\vec{OR}_{SP}$ is reffered to below as $\widehat{X_{R_{SP}}}$. The sign of

$$\Delta = \frac{\partial^2 h}{\partial\theta_R^2}\cdot\frac{\partial^2 h}{\partial\Gamma^2(\vec{X_M})} - \left(\frac{\partial^2 h}{\partial\theta_R\partial\Gamma(\vec{X_M})}\right)^2$$

is then studied. Lastly for every pair $(\theta_{R_{SP}}, \vec{X_{M_{SP}}})$ such that $\Delta \neq 0$, the 2-D stationary phase method gives

$$\Phi(\vec{\xi}, k_1) = \frac{2\pi}{k_1}\frac{g(\theta_{R_{SP}}, \vec{X_{M_{SP}}})}{\sqrt{|\Delta|}} \cdot \mathrm{e}^{+\mathrm{j}k_1 h(\theta_{R_{SP}}, \vec{X_{M_{SP}}})}\, \mathrm{e}^{\mathrm{j}\,\mathrm{sign}(\Delta)\frac{\pi}{4}}. \quad (19)$$

After some calculations (cf. the Appendix), substituting (19) into (15) gives

$$\tilde{f_{SP}}(\vec{\xi}) = 2\pi\left[1+\cos(\theta_T-\theta_{R_{SP}})\right]\|\widehat{X_T}+\widehat{X_{R_{SP}}}\| \cdot R_c(\vec{X_{M_{SP}}}) \int_{k_0-\frac{\Delta k}{2}}^{k_0+\frac{\Delta k}{2}} \frac{\mathrm{e}^{\mathrm{j}\left\{k_1\left[\widehat{X_T}+\widehat{X_{R_{SP}}}\right]\cdot\left[X_{\vec{M}_{SP}}-\vec{\xi}\right]+\mathrm{sign}(\Delta)\frac{\pi}{4}\right\}}}{\sqrt{|\Delta|}}\, \mathrm{d}k_1. \quad (20)$$

In the case where image pixels are located inside the target area, no solution is obtained because the stationary points are degenerated when $\Delta = 0$. When image pixels are located outside the target area i.e. when $\Delta < 0$, substituting the integral into (20) involves

$$\tilde{f_{SP}}(\vec{\xi}) = \frac{2\mathrm{e}^{-\mathrm{j}\frac{\pi}{4}}\pi\Delta k\left[1+\cos(\theta_T-\theta_{R_{SP}})\right]\|\widehat{X_T}+\widehat{X_{R_{SP}}}\|R_c(\vec{X_{M_{SP}}})}{\sqrt{|\Delta|}} \cdot \mathrm{sinc}\left(\frac{\Delta k}{2}\left[\widehat{X_T}+\widehat{X_{R_{SP}}}\right]\cdot\left[\vec{X_{M_{SP}}}-\vec{\xi}\right]\right) \cdot \mathrm{e}^{-\mathrm{j}k_0\left[\widehat{X_T}+\widehat{X_{R_{SP}}}\right]\cdot\left[X_{\vec{M}_{SP}}-\vec{\xi}\right]}, \quad (21)$$

with $(\widehat{X_T}+\widehat{X_{R_{SP}}}) \neq \vec{0}$, the image given by $\tilde{f_{SP}}(\vec{\xi})$ reaches its maximum for $\vec{\xi} = \vec{X_{M_{SP}}}$, i.e. for image pixels which are located on target boundary. This function is therefore called "shape function" . This feature is used to obtain an imaging algorithm giving the shape of targets under KA assumptions. From (10),

$$v^d(\widehat{X_T}+\widehat{X_R}, k_1) = 8\pi\frac{\sqrt{\|\vec{X_T}\|\,\|\vec{X_R}\|}\,\mathrm{e}^{\mathrm{j}k_1(\|\vec{X_T}\|+\|\vec{X_R}\|)}\,P_0^*(f)}{|P_0(f)|^2}\,P^d(\vec{X_R}, k_1). \quad (22)$$

Equations (22) and (14) involve

$$\tilde{f}(\vec{\xi}) = 8\pi\int_{k_0-\frac{\Delta k}{2}}^{k_0+\frac{\Delta k}{2}}\int_{\theta_{R_{min}}}^{\theta_{R_{max}}} k_1\left[1+\cos(\theta_T-\theta_R)\right] \cdot\sqrt{\|\vec{X_T}\|\,\|\vec{X_R}\|}\,\mathrm{e}^{\mathrm{j}k_1(\|\vec{X_T}\|+\|\vec{X_R}\|)} \cdot\frac{P_0^*(f)}{|P_0(f)|^2}\,P^d(\vec{X_R}, k_1)\,\mathrm{e}^{-\mathrm{j}\vec{k}\cdot\vec{\xi}}\,\mathrm{d}\theta_R\,\mathrm{d}k_1. \quad (23)$$

As with the MFA, the algorithm is first presented in the case where there are one transmitter located at T and N_R receivers located at R_m. The discrete values of θ_R are reffered to below as θ_{R_m}.

Discretization of (23), which gives the amplitude $I_K(\vec{\xi})$ of each image pixel P, yields

$$I_K(\vec{\xi}) = 8\pi\sum_{l=1}^{N_f}\sum_{m=1}^{N_R} k_{1_l}\left[1+\cos(\theta_T-\theta_{R_m})\right] \cdot\sqrt{\|\vec{X_T}\|\,\|\vec{X_{R_m}}\|}\,\mathrm{e}^{\mathrm{j}k_{1_l}\left(\|\vec{X_T}\|+\|\vec{X_{R_m}}\|\right)} \cdot\frac{P_0^*(f_l)}{|P_0(f_l)|^2}\,P^d(\vec{X_{R_m}}, k_{1_l})\,\mathrm{e}^{-\mathrm{j}\vec{k_{l,m}}\cdot\vec{\xi}}\,\frac{2\pi\delta f}{c_1}\,\delta\theta_R, \quad (24)$$

Where δf denotes the frequency step and $\delta\theta_R$ the angle step. The implementation of the IRAKA is performed on the frequency samples where the transmitted signal is not equal to zero to avoid instability problems due to the division of $|P_0(f_l)|^2$.

As in the case of the MFA, (24) can be used to reconstruct an image with one transmitter and several receivers. To obtain the multistatic image, a coherent sum of these images is performed.

Equations (5) and (24) show that both algorithms have the same mathematical kernel and consequently the same computational complexity. However, the IRAKA includes a spatio-frequency filter denoted

$$H(\theta_T, \theta_R, f) = \frac{2\pi f}{c_1}\left[1 + \cos(\theta_T - \theta_R)\right].$$

$H(\theta_T, \theta_R, f)$ depends on the frequency range and on the transducer locations. The bistatic angle (as referred to below as β) is the angle between $\vec{X_T}$ and $\vec{X_R}$. Thus, $H(\theta_T, \theta_R, f) = H(\beta, f) = 2\pi f[1 + \cos(\beta)]/c_1$.

Comparing the MFA and the IRAKA, we can give following comments: for the MFA (5) appears a pulse compression: the multiplication of the received signal by $P_0^*(f)$ for each frequency with the division of the total intensity by the total energy of the transmitted signal. This process, intrinsic to the target model and to the inversion operation, allows to improve the SNR. For the IRAKA (24), only appears a deconvolution operation: it is given by the multiplication of the received signal by $P_0^*(f)/|P_0(f)|^2$ for each frequency.

From (21), it can be noted that the shape function holds quantitative information on target via the reflexion coefficient $R_c(\vec{X_M})$. Before studying capabilities of the IRAKA to reconstruct quatitative information, it must be checked to prove its capability to reconstruct target shape.

5. Comparisons between the IRAKA and the MFA: Simulations and tank experiments

In this part, images reconstructed by performing the MFA and the IRAKA are first compared in a simulation context and then in a tank experimental context. These comparisons focus on the quality of shape reconstruction. For the sake of comparisons, the images are normalized with respect to their maximum. The signals transmitted are slightly different between simulations and experiments but "short pulses" are used in both cases in order to ensure good image resolution. A specific multistatic configuration is chosen to test the algorithms. A possible operational multistatic configuration for SAS applications will be presented in part 6. The $k_0 a$ ranges between 10 and 20. There is no receiver in the target shadow and so no receiver is located in the forward direction. In addition, $k_0\, L_T(\vec{\xi}) \approx 1000 \gg 1$ and $k_0 L_R(\vec{\xi}) \approx 1000 \gg 1$ which is in agreement with the far field assumption.

5.1. Results of simulations in a multistatic context

Images shown in this section are reconstructed from numerical data. These data correspond to the field diffracted by the 2-D target of circular cross-section or the 2-D target of elliptic cross-section. These two solid targets are made of stainless steel. Numerical data are computed using a modal series for the 2-D target of circular cross-section [18] and Boundary Element Method (BIE) for the 2-D target of elliptic cross-section [19]. The data used in this subsection are noiseless.

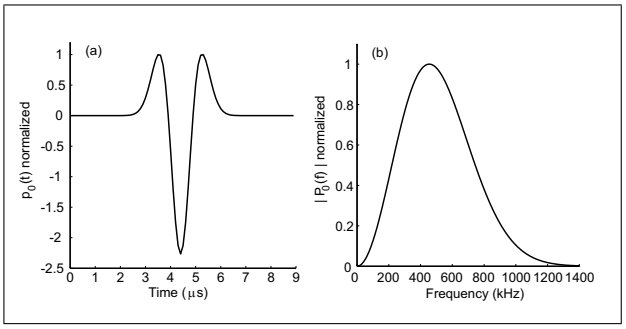


Figure 2. Analytical transmitted signal called Ricker. a: Transmitted signal in simulation, b: Transmitted signal spectrum in simulation.

5.1.1. Simulation context and parameters

The transmitted signal $p_0(t)$ used in the simulations is a Ricker impulse with its spectrum $P_0(f)$ shown in Figure 2. Its central frequency is $f_0 = 500\,\text{kHz}$ and its bandwith at $-3\,\text{dB}$ is $B_{-3\text{dB}} = 375\,\text{kHz}$. Water density is $\rho_1 = 1000\,\text{kg/m}^3$ and sound speed in the water is $c_1 = 1480\,\text{m/s}$ ($\lambda_0 \approx 0.3\,\text{cm}$).

In this part, the multistatic configuration is divided into 8 bistatic configurations, each composed of one transmitter and 91 receivers. The multistatic configuration is composed of 8 transmitters, the locations of which can be seen in Figure 3a.

The first bistatic configuration is shown in Figure 3b. In this configuration, the transmitter is located at $\theta_T = 45°$ and the 91 receivers are located from 0° to 90°, every degree. To obtain the second bistatic configuration, a 45° rotation of all the transducers of the first bistatic configuration is performed. This rotation is repeated each time, giving the 8 bistatic configurations.

The MFA and the IRAKA are then used to obtain the 8 bistatic images from these configurations. With each algorithm, the 8 bistatic images are coherently summed to obtain the multistatic image. Only multistatic images are presented here.

In the simulations, the 2-D target of circular cross-section is taken to be $1\,\text{cm}$ ($\approx 3.33\lambda_0$) in diameter and the 2-D target of elliptic cross-section is taken to measure $2\,\text{cm}$ ($\approx 6.67\lambda_0$) in the direction of the large axis and $1\,\text{cm}$ ($\approx 3.33\lambda_0$) in that of the small axis. The target is centered on the geometrical center O. The distance from the transducers to the geometrical center O is set as $\|\vec{X_T}\| = \|\vec{X_{R_m}}\| = 50\,\text{cm}$ ($\approx 167\lambda_0$).

Numerical values of the physical parameters are as follows: $\rho_2 = 7900\,\text{kg/m}^3$, $c_s = 3100\,\text{m/s}$ and $c_p = 5790\,\text{m/s}$.

5.1.2. Effects of the filter $H(\beta, f)$

From the frequency range and the transducer locations previously given, the effects of the filter $H(\beta, f) = 2\pi f[1 + \cos(\beta)]/c_1$ present in the IRAKA but not in the MFA can be studied. In any bistatic configuration $|\beta|$ ranges between 0 and 45°. Figure 4 gives the effects of the filter $H(\beta, f)$ on $P_0(f)$ as a function of β and f in the 0 to $1.2\,MHz$ frequency range.

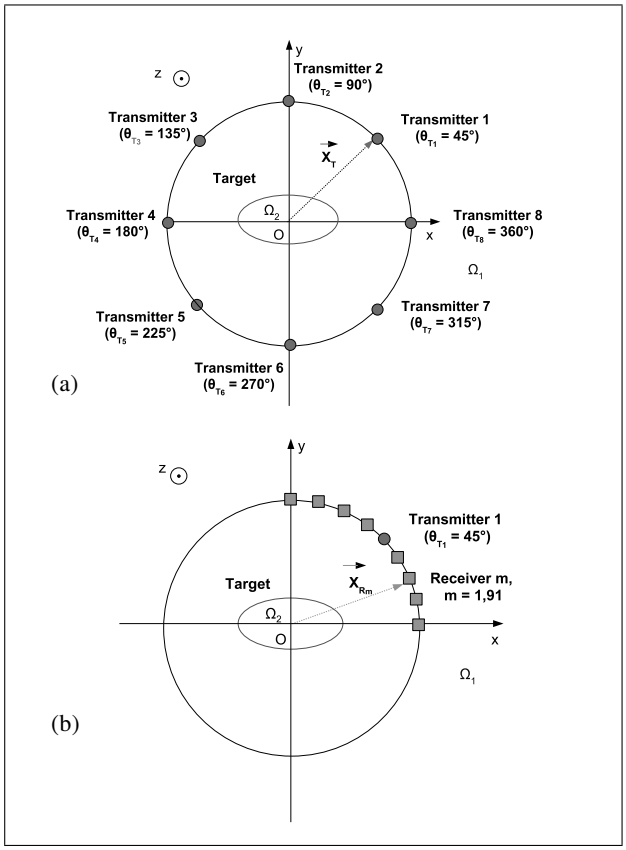


Figure 3. Multistatic configuration. a: Transmitter locations, b: first bistatic configuration.

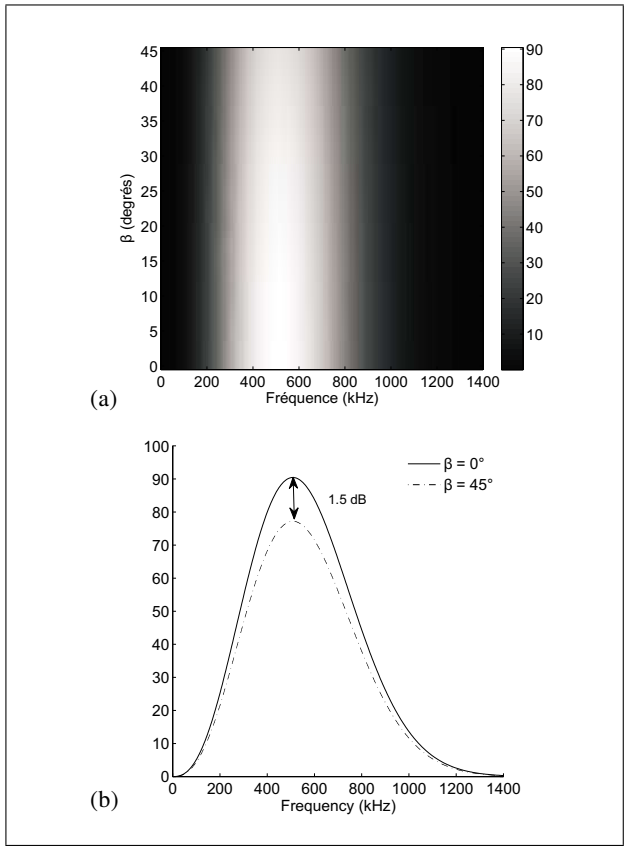


Figure 4. $P_0(f)$ filtered by $H(\beta, f)$. a: Effects of $H(\beta, f)$ for $\beta = 0$ to 45°, b: Effects of $H(\beta, f)$ for $\beta = 0$ and $\beta = 45°$.

From Figure 4a, it can be deduced: the smaller the bistatic angle, the greater the filtered transmitted signal spectrum. The filter therefore increases the amplitude of the signals received at small bistatic angles. The difference between the maximum of $|P_0(f)|$ values filtered by $H(\beta, f)$ at the smallest and the highest bistatic angles is found at about 1.5 dB on Figure 4b. Since this difference is quite small, it can be assumed that it would have little influence on image reconstructed with the IRAKA.

5.1.3. Reconstructed images based on numerical data

Target images are reconstructed with both the MFA and the IRAKA. Figure 5 shows multistatic images of the 2-D target of circular cross-section reconstructed with the MFA (a) and with the IRAKA (b). Figure 6 shows multistatic images of the 2-D target of elliptic cross-section, reconstructed with the MFA (a) and with the IRAKA (b).

First, it can be observed Figure 5 and Figure 6 that the circular and the elliptic shapes of the 2-D targets are reconstructed for both algorithms. (Ox) and (Oy) cuttings of the MFA and the IRAKA images are shown in Figure 7 and Figure 8 for the sake of comparison. Two criteria are chosen to compare MFA and IRAKA in terms of quality of the target shape reconstruction. The first criterion is the error Erx along (Ox) or Ery along (Oy) between the location of the maximum amplitude and the actual value of the target boundary. The second criterion is the thickness $\Delta x_{-3\text{dB}}$ along (Ox) or $\Delta y_{-3\text{dB}}$ along (Oy) of the boundary at -3 dB of the maximum amplitude peak.

Table I. Criteria of target shape reconstruction in simulation. Erx and Ery in %, $\Delta x, y$ in cm.

Shape	Algorithm	Erx	Ery	$\Delta x_{-3\text{dB}}$	$\Delta y_{-3\text{dB}}$
circular	MFA	4	4	0.043	0.043
circular	IRAKA	2	2	0.020	0.020
elliptic	MFA	2	2	0.126	0.110
elliptic	IRAKA	0	0	0.053	0.046

The results for criteria obtained from (Ox) and (Oy) cuttings are shown in Table I.

It can be deduced from these results that the IRAKA gives better results than the MFA for target shape reconstruction under criteria chosen for both target shapes studied.

5.2. Experimental tank results in a multistatic context

5.2.1. Experimental tank context and parameters

The multistatic tank experimental data acquisition system used here is composed of two Panametrics V301 transducers working at 500 kHz. These are directional transducers with a 7° aperture. One of them is used as a transmitter and the other as a receiver. The receiver could be moved

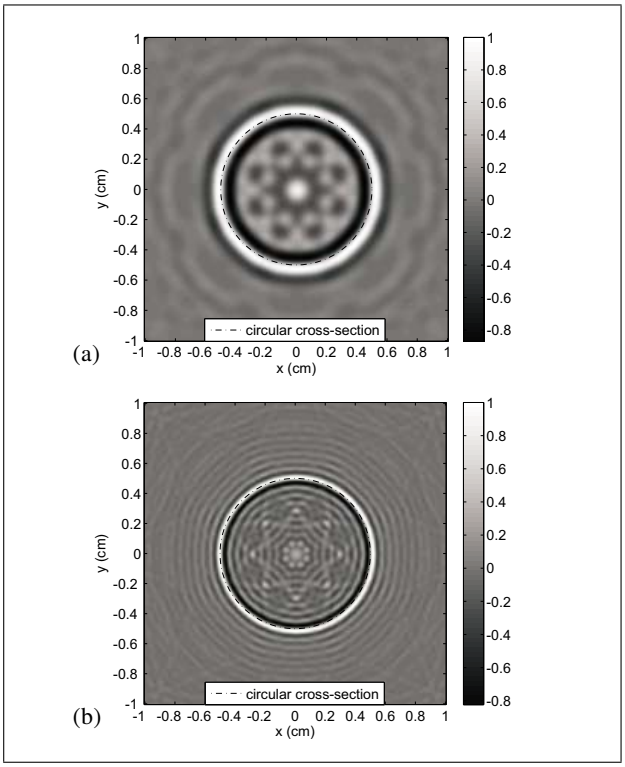


Figure 5. Multistatic images of the 2-D target of circular cross-section. a: MFA image, b: IRAKA image.

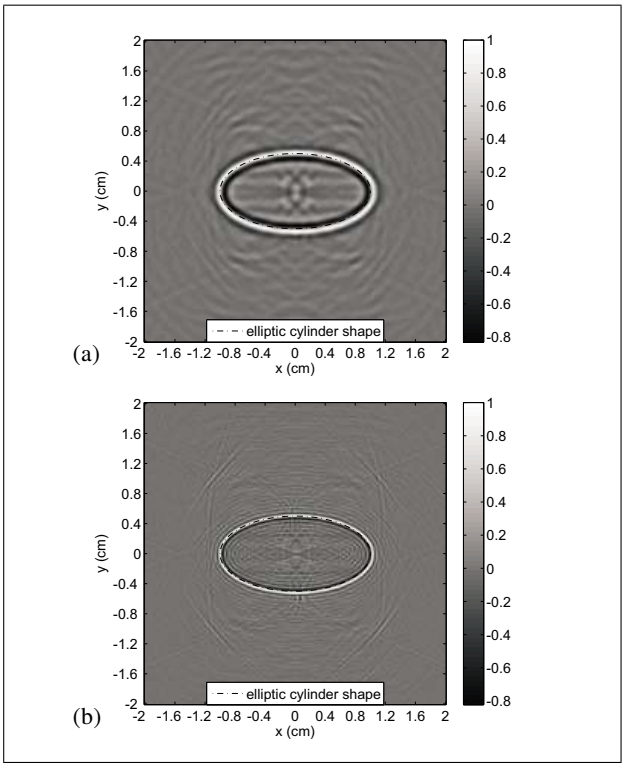


Figure 6. Multistatic images of the 2-D target of elliptic cross-section. a: MFA image, b: IRAKA image.

between two data acquisitions in order to simulate an array. In this part, $p_0(t)$ is the signal transmitted and received by the two transducers. This signal and its spectrum are

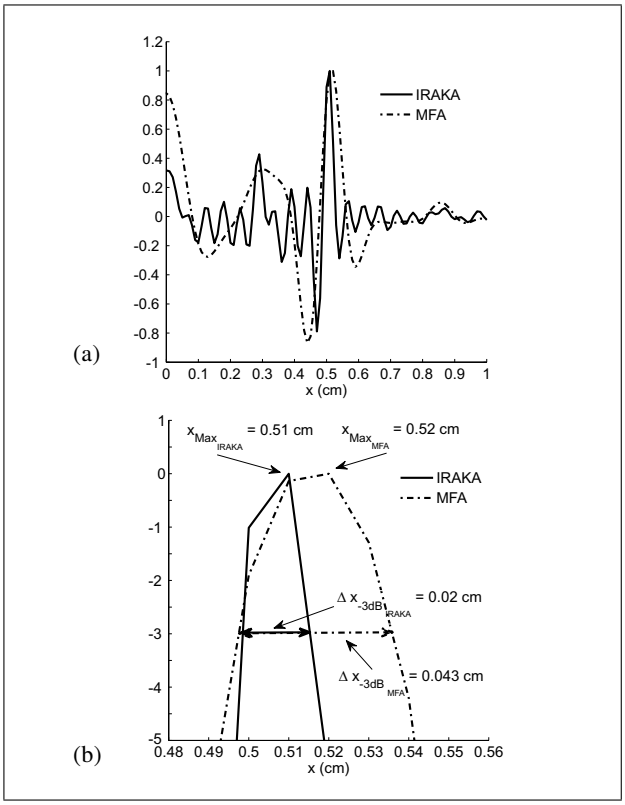


Figure 7. (Ox) cuttings of the 2-D target of circular cross-section images reconstructed with the IRAKA and the MFA using numerical data. a: (Ox) cutting, b: Criteria for shape reconstruction.

shown in Figure 9. Its central frequency is $f_0 = 500\,\text{kHz}$ and its bandwith at $-3\,\text{dB}$ is 220 kHz. The first target is a solid circular stainless steel 2-D target 1 cm ($\approx 3.33\lambda_0$) in diameter. The second target is a solid elliptic stainless steel 2-D target measuring 1.2 cm ($\approx 4\lambda_0$) in the direction of small axis and 2.4 cm ($\approx 8\lambda_0$) in the direction of large axis. Water density is $\rho_1 = 1000\,\text{kg/m}^3$ and sound speed in water is about $c_1 = 1477\,\text{m/s}$.

The experimental multistatic configuration is run under the same conditions as in simulations, apart from some details due to experimental constraints: the transmitter and the receiver can not be located on the same circle and no data are available when the receiver is in the shadow of the transmitter i.e. between $-5\,^\circ$ and $+5\,^\circ$ around the transmitter. The distance between the transmitter and the geometrical center is $\|\vec{X}_T\| = 33.4\,\text{cm}$ ($\approx 111\lambda_0$) and the distance between the receiver and the geometrical center is $\|\vec{X}_R\| = 44.3\,\text{cm}$ ($\approx 148\,\lambda_0$). Distances $L_T(\vec{\xi})$ and $L_R(\vec{\xi})$ between transducers and target area are more than 30 cm ($\approx 100\lambda_0$) which is large enough to be under far field conditions: $k_0 L_T(\vec{\xi}) \gg$ and $k_0 L_R(\vec{\xi}) \gg 1$. Signals reflected from the tank walls and from the air-water interface are removed from the data using a time-filtering procedure in order to simulate a free space experiment.

5.2.2. Images reconstructed from tank experimental data

Figure 10 and Figure 11 respectively shows multistatic images of the 2-D target of circular cross-section and the 2-D

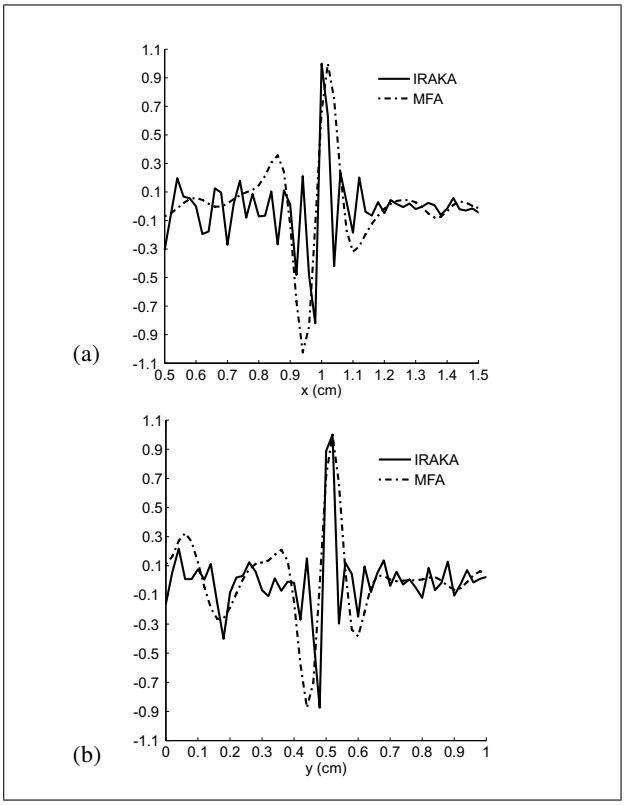


Figure 8. 2-D target of elliptic cross-section - Comparison between cuttings of MFA/IRAKA images along the (Ox) and (Oy) axis - Numerical data. a: (Ox) cutting, b: (Oy) cutting.

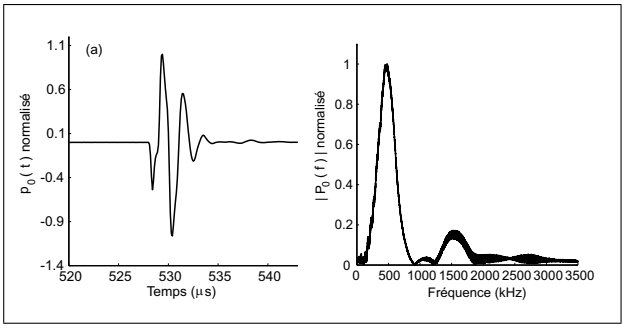


Figure 9. Signal after transmission and reception by transducers.

target of elliptic cross-section reconstructed with the MFA in (a) and with the IRAKA in (b) using tank experimental data.

First, it can be seen that the shapes of the 2-D targets of circular and elliptic cross-sections are reconstructed with both algorithms which confirms simulation results. In this tank experiment, as it can be seen from Figures 10 and 11, the target is placed near the geometrical center but not precisely at the geometrical center.

This tank experiment shows that it is possible to reconstruct target shapes with both algorithms in an experimental context and the same conclusions can be made as in the simulations. In terms of noise robustness, the SNR level was about 40 dB in the experimental tank. For this experiment, both algorithms allow to reconstruct target shape but

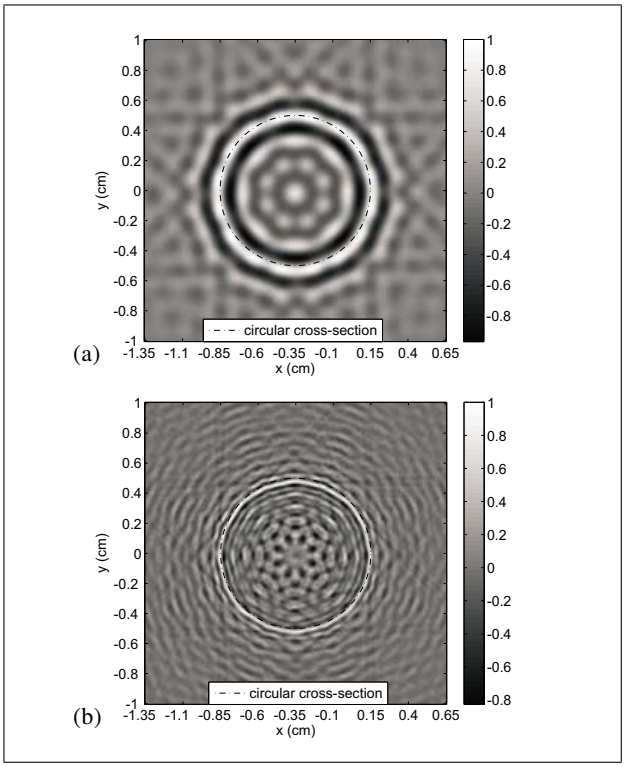


Figure 10. Multistatic images of the 2-D target of circular cross-section - Tank experimental data. a / b: MFA / IRAKA image.

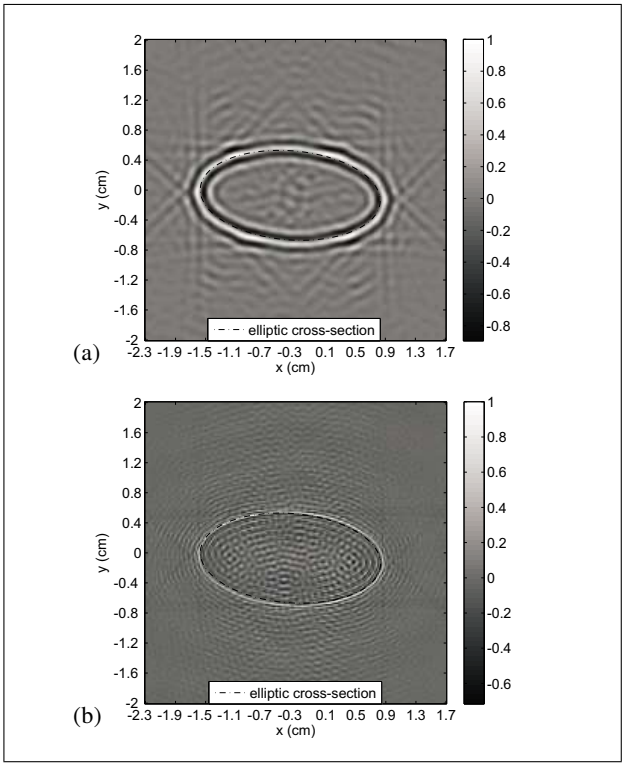


Figure 11. Multistatic images of the 2-D target of elliptic cross-section - Tank experimental data. a / b: MFA / IRAKA image.

we wonder if it is also the case when the SNR is smaller than 40 dB. A study is thus performed to compare algo-

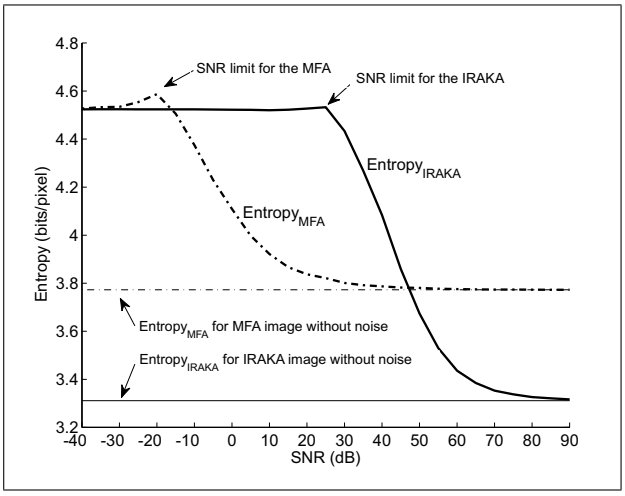


Figure 12. Evolution of the image entropy in function of the SNR for MFA and IRAKA without the stabilization deconvolution method.

rithms in terms of noise robustness in the following subsection.

5.3. Simulation results in a multistatic context in presence of noise

In this sub-section, MFA and IRAKA are compared in terms of noise robustness. A white gaussian circular noise is added to numerical data with different SNR levels and limits for both algorithms are presented. MFA should be the best robust of both algorithms because it maximises the SNR in presence of additive white gaussian noise. In order to quantify the SNR limit of target detection in the noise, calculations of images entropy are performed every 5 dB of SNR from -40 to 90 dB. Image entropy allows to evaluate the quantity of information by pixel on the image. It is usually used in image processing to edge detection [20]. The Figure 12 shows the evolution of the image entropy in function of the SNR for MFA and IRAKA.

On the one hand, when the SNR is sufficiently high i.e. 60 dB for the MFA and 90 dB for the IRAKA, the entropy becomes constant and is equal to the image entropy without noise. On the other hand, when the SNR decreases and the entropy stops increasing to tend to a constant value, it means that the target is not visible any more and that there is only noise on the image. From these curves, the SNR limits can be found at about -20 dB for the MFA and 25 dB for the IRAKA. Images of the 2-D target of circular cross-section at these SNR limits are presented Figure 13a for the MFA and Figure 13b for the IRAKA. From these results, it can be deduced that the MFA is more robust to additive white gaussian noise compared to the IRAKA in this context of simulation. The feature responsible for this lack of noise robustness in the IRAKA has been identified to be the step of deconvolution.

One simple method can be used to stabilize the step of deconvolution in the IRAKA [21]. This method consists in replacing $|P_0(f)|^2$ by

$$\mathrm{Max}\{|P_0(f_l)|^2, c \cdot \mathrm{Max}[|P_0(f_l)|^2]\}/W(f_l)$$

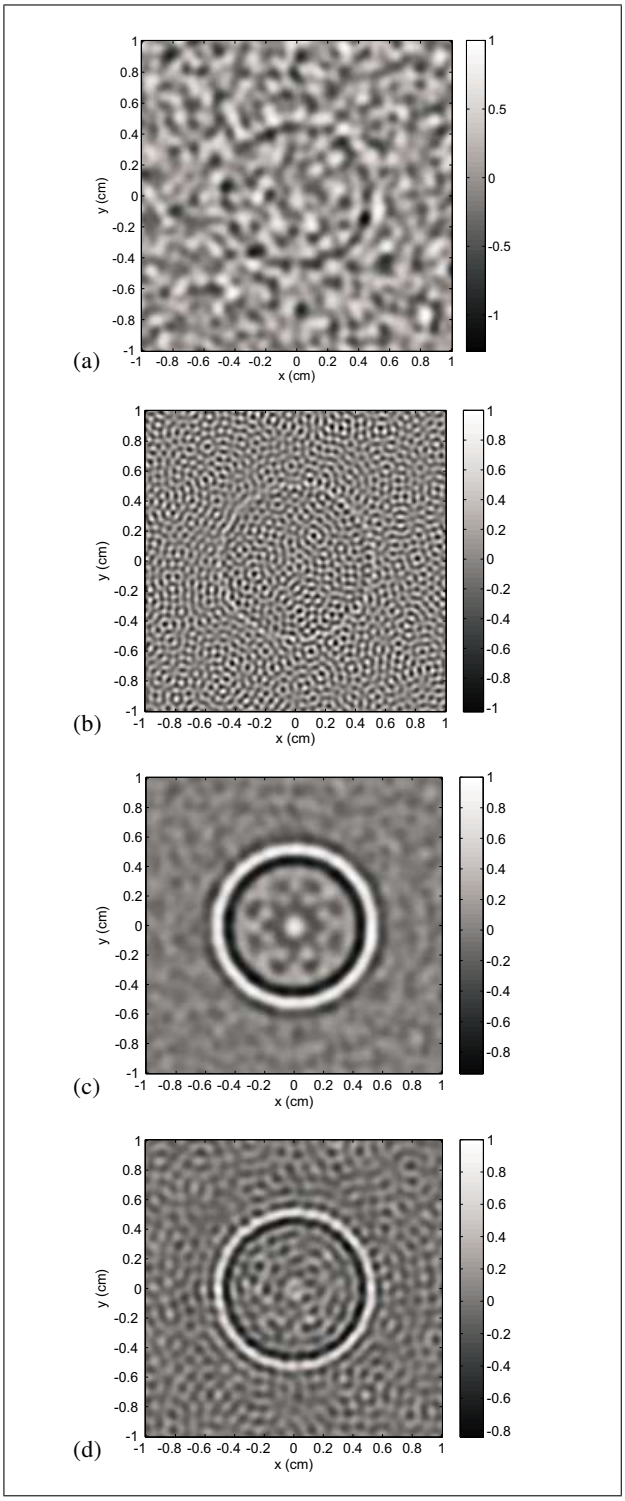


Figure 13. Multistatic images of the 2-D target of circular cross-section - Numerical results with additive circular white gaussian noise. a: MFA image at SNR = -20 dB, b: IRAKA image at SNR = 25 dB without the stabilization deconvolution method, c: MFA image at SNR = 0 dB, d: IRAKA image with the stabilization deconvolution method at SNR = 0 dB.

in (24). With $c \approx 0.05$ and $W(f)$ the bandpass filter which cutting frequencies are such that

$$|P_0(f)|^2 > c \cdot \mathrm{Max}\left[|P_0(f)|^2\right].$$

Images are reconstructed with the MFA at SNR = 0 dB on the Figure 13c and with the IRAKA implemented with the stabilization deconvolution method (SDM) described above which amplitude is denoted by I_{KSDM} on the Figure 13d. These images show that the IRAKA provides a narrower boundary than the IRAKA at sufficiently low SNR in view of sea experiments.

6. Comparisons between IRAKA and MFA in tank experiments using a multistatic forward looking SAS

In the last part of this study, images of a 2-D target of circular cross-section are reconstructed from tank experimental data performed with a multistatic forward looking SAS. This configuration is more suitable for underwater acoustics applications than the previous one. In addition, in order to be in the context of mines detection and identification in terms of $k_1 a \approx 40$, the central frequency of the signal selected is taken higher whereas the target size is the same as in the previous tank experiment. In this part, the application hypothesis of the IRAKA and the MFA are also respected.

6.1. Experimental tank context and parameters

The multistatic experimental acquisition system is shown in Figure 14. The target is a solid circular stainless steel 2-D target $1\,cm\,(\approx 14.3\ \lambda_0)$ in diameter, immersed in an experimental tank. The transducer system is composed of one Imasonic transducer used as a transmitter and an omnidirectional transducer used as a receiver. The Imasonic transducer is directional with a 6 ° aperture, the receiver is an omnidirectional tranducer. The transmitter insonifies the target area with a grazing angle of $\theta_0 = 40°$. The receiver is moved after each data acquisition. There are $N_R = 67$ receiver locations. The 2-D target of circular cross-section is insonified by a short signal which is shown Figure 15 after being transmitted and received by the transducers used. Its central frequency is $f_0 = 27$ MHz and the bandwith at -3 dB is 720 kHz (cf. Figure 15). Water density is $\rho_1 = 1000\,\mathrm{kg/m^3}$ and water sound speed is about $c_1 = 1482$ m/s, so that $k_0 a \approx 42$ and $\lambda_0 \approx 7 \cdot 10^{-2}$ cm.

The distance between the transmitter and the geometrical center is $\|\vec{X_T}\| = 25.9$ cm $(\approx 350\lambda_0)$ and the distance between the receiver 1 and the geometrical center is $\|\vec{X_{R_1}}\| = 38$ cm $(\approx 514\,\lambda_0)$. The same tank experiment is repeated with a grazing angle θ_0 of 30°. The multistatic image is reconstructed from experiments data at both $\theta_0 = 40°$ and $\theta_0 = 30°$. The distances $L_T(\vec{\xi})$ and $L_R(\vec{\xi})$ are about 35 cm $(\approx 500\ \lambda_0)$.

6.2. Effects of the filter $H(\beta, f)$

In this study, $|\beta|$ varies from approximately 70° to 100°. Figure 16 shows the effects of the filter $H(\beta, f)$ on the spectrum of the transmitted signal shown in Figure 15b. Upon comparing Figures 15b and 16b it can be seen that

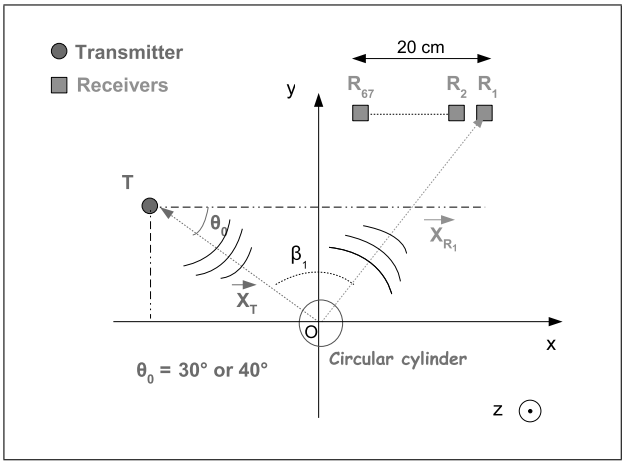


Figure 14. Configuration of the multistatic forward looking SAS.

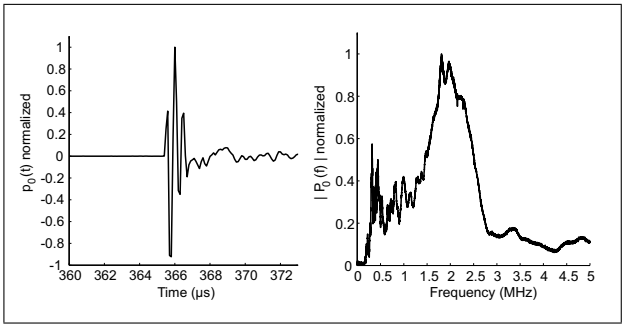


Figure 15. Signal after transmission and reception by transducers.

the filter attenuates the low frequencies of the signal $P_0(f)$ i.e. those ranging between 200 kHz and 1.2 MHz.

The difference between the maximum values of the transmitted signal spectrum filtered by $H(\beta, f)$ at the lowest and highest bistatic angles is approximately 5 dB. This difference is larger than in previous simulations and experiments because the frequency is higher there than in the previous study.

6.3. Images reconstructed using a multistatic forward looking SAS

The 2-D target of circular cross-section is reconstructed as shown in Figure 17 with the MFA in (a) and the IRAKA in (b).

As it can be seen in these images, only a little part of the 2-D target shape is reconstructed in this case, because there are only two insonification directions. Under these experimental conditions, the IRAKA and the MFA give very similar results: the effects of the filter are not clearly visible on the IRAKA image. Looking at the consequences of three different processings on a received signal Figure 18, it can be seen that deconvolution increases perturbations in the last part of the received signal more than pulse compression does. This feature is also visible on IRAKA and MFA images comparing Figure 17a and b. From Figure 18, it can be noted that the filter $H(\beta, f)$

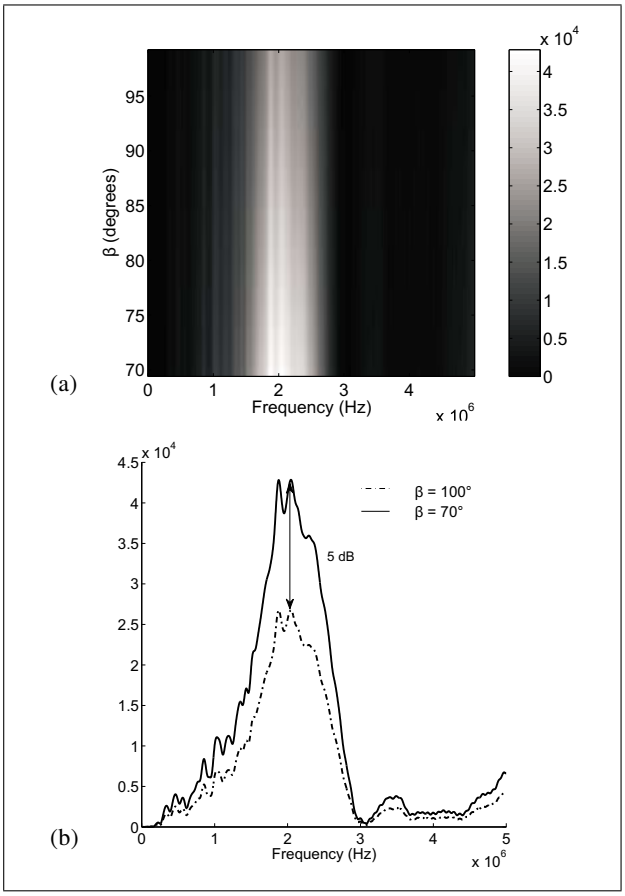


Figure 16. $P_0(f)$ filtered by $H(\beta, f)$ - Forward looking SAS tank experimental data.

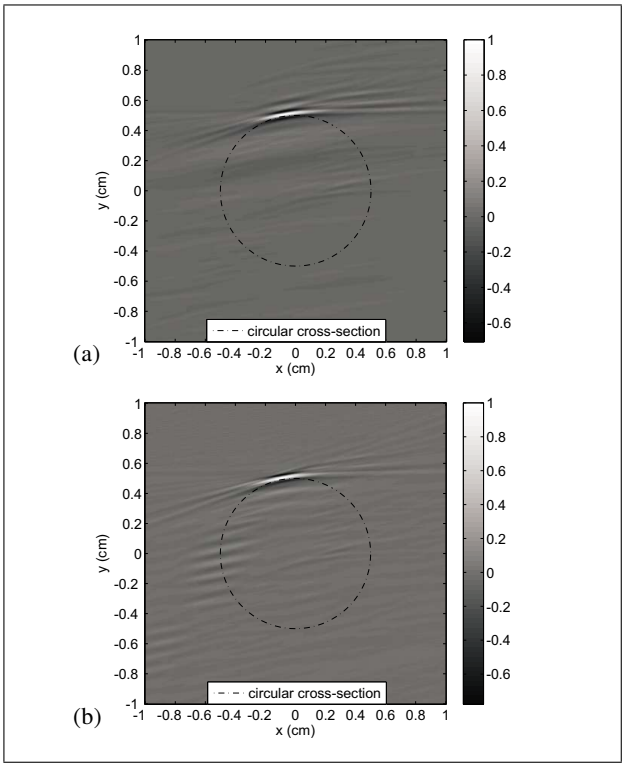


Figure 17. Multistatic images of the 2-D target of circular cross-section. Forward looking SAS tank experimental data. MFA and IRAKA image.

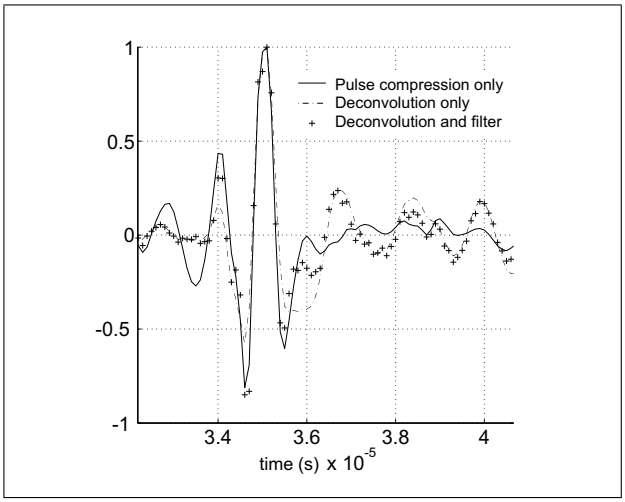


Figure 18. Effects of compression, deconvolution and filtering by $H(\beta, f)$ on the first signal received.

and deconvolution combinated have almost the same effect than deconvolution only.

7. Discussion

In this paper, two imaging methods are compared: the MFA based on the "point scatterers" model of the target and the IRAKA based on the KA of the scattered field. The difference between the forward models of the scattered field for each method lies on a geometrical term present in the KA model which depends on the bistatic configuration. It results that the model based on the KA is more comprehensive than the "point scatterers" model. The IRAKA is established to reconstruct target shapes. It is compared to the MFA that is classicaly used to reconstruct target images in radar and sonar. The 2-D stationary phase method applyied to the IRAKA provides a function called "shape function" that is maximal on the target boundary and that depends on the reflexion coefficient.

The mathematical differences between these imaging methods are a spatio-frequency filtering and a deconvolution involved in the IRAKA, as compared with a pulse compression alone in the MFA. It can be noted that the deconvolution present in the IRAKA provides a better quality of target shape reconstruction but also a lack of robustness to noise. A simple method to stabilize the deconvolution has been proved efficient to improve the algorithm robustness to additive white gaussian noise at sufficiently low SNR.

The IRAKA could be used to obtain quantitative information about the target as the shape function depends on the target reflection coefficient. Quantitative reconstruction performances of the IRAKA are now under investigation.

In this study, the IRAKA has been developed to deal with targets in a homogeneous environement, but this

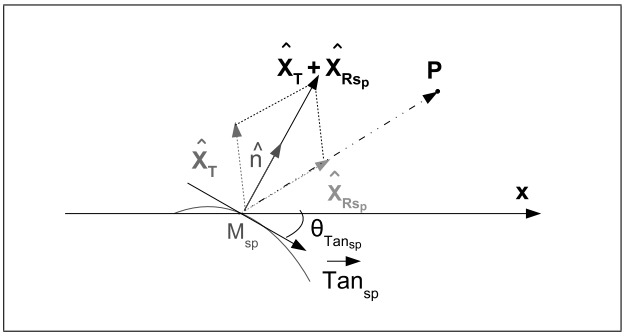


Figure A1. Vectors under stationary conditions.

method could be extended to more complex situations and in particular to the case of buried targets in sediments.

Appendix

Stationary conditions are studied in details in this appendix. Figure A1 gives the vectors involved in the case of stationary conditions.

On the one hand, $\partial h/\partial\Gamma(\vec{X_M}) = 0$ involves that $\left(\widehat{X_T} + \widehat{X_{R_{SP}}}\right) \cdot \vec{Tan}_{SP} = 0$.

This is to say that $(\widehat{X_T} + \widehat{X_{R_{SP}}})$ is colinear to $\hat{n}$.

On the other hand, $\partial \vec{X_{R_{SP}}}/\partial\theta_{R_{SP}} \cdot (\vec{X_{M_{SP}}} - \vec{\xi}) = 0$.

This is to say that $\widehat{X_{R_{SP}}}$ is colinear to $(\vec{X_{M_{SP}}} - \vec{\xi})$.

Here $\vec{Tan}_{SP} = \partial \vec{X_{M_{SP}}}/\partial\Gamma(\vec{X_{M_{SP}}})$ is the tangent vector on M_{SP}.

Note that: $\hat{n} = \chi_{SP}\, \partial \vec{Tan}_{SP}/\partial\Gamma(\vec{X_{M_{SP}}})$, where χ_{SP}, which is the curvature of the target boundary at point M_{SP}, is strictly positive.

From $\partial h/\partial\Gamma(\vec{X_M}) = 0$, for a given transmission direction $\widehat{X_T}$ and reception direction $\widehat{X_{R_{SP}}}$, the point M that reflects the maximal energy is found for $\hat{n}//(\widehat{X_T} + \widehat{X_{R_{SP}}})$ and is denoted M_{SP}. As the target is convex because of the KA hypothesis, and as the Physical Optics approximation hypothesis means that only the contribution of the insonified part of the target has to be taken into account, this point M_{SP} is unique for both the reception direction $\theta_{R_{SP}}$ and the transmission direction $\widehat{X_T}$ given.

Δ is calculated here and its sign is studying:

$$\Delta = -\chi_{SP}\alpha_{SP} \|\widehat{X_T} + \widehat{X_{R_{SP}}}\| \, \|\vec{X_{M_{SP}}} - \vec{\xi}\| - \left[\sin\left(\theta_{\vec{Tan}_{SP}} - \theta_{R_{SP}}\right)\right]^2, \quad \text{(A1)}$$

where $\theta_{\vec{Tan}_{SP}}$ is the angle between $\vec{Tan}_{SP}$ and $(O\vec{x})$ axis,

$\alpha_{SP} = 1$ with $\vec{M_{SP}P}$ toward the outgoing normal and $\alpha_{SP} = -1$ in the opposite case.

There are two cases depending on the direction of $\vec{M_{SP}P}$:

- If the $\vec{M_{SP}P}$ vector is toward the outgoing normal, then $\Delta < 0$.
- If the $\vec{M_{SP}P}$ vector is toward the ingoing normal, then there three cases arise:

$$\|\vec{X_{M_{SP}}} - \vec{\xi}\| < \frac{\left[\sin\left(\theta_{\vec{Tan}_{SP}} - \theta_{R_{SP}}\right)\right]^2}{\chi_{SP}\,\|\widehat{X_T} + \widehat{X_{R_{SP}}}\|} \Rightarrow \Delta < 0,$$

$$\|\vec{X_{M_{SP}}} - \vec{\xi}\| = \frac{\left[\sin\left(\theta_{\vec{Tan}_{SP}} - \theta_{R_{SP}}\right)\right]^2}{\chi_{SP}\,\|\widehat{X_T} + \widehat{X_{R_{SP}}}\|} \Rightarrow \Delta = 0,$$

$$\|\vec{X_{M_{SP}}} - \vec{\xi}\| > \frac{\left[\sin\left(\theta_{\vec{Tan}_{SP}} - \theta_{R_{SP}}\right)\right]^2}{\chi_{SP}\,\|\widehat{X_T} + \widehat{X_{R_{SP}}}\|} \Rightarrow \Delta > 0.$$

References

[1] R. Birk, W. Camus, E. Valenti, W. McCandless: Synthetic aperture radar imaging systems. IEEE AES Systems Magazine **10** (1995) 15–23.

[2] A. Hetet: Contribution à la détection de mines enfouies dans le sédiment marin par synthèse d'ouverture basse fréquence. Thesis, University Paris 6, Mecanics, 2003.

[3] F. Daout, G. Ginolhac, F. Schmitt, M. Lesturgie: Passive bistatic imagery of targets modelled by NEC. International Conference on Radar Systems, Toulouse, September 2004.

[4] J. R. Edwards, H. Schmidt, K. LePage: Bistatic synthetic aperture target detection and imaging with an AUV. IEEE Journal of Oceanic Engineering **26** (2001) 690–699.

[5] M. Soumekh: Synthetic aperture radar signal processing with Matlab algorithms. Wiley-Interscience, 1999.

[6] H. J.Callow: Signal processing for synthetic aperture sonar image enhancement. Thesis, University of Canterbery, Electrical and Electronic of Engineering, 2003.

[7] B. D. Rigling, R. L. Moses: Polar format algorithm for bistatic SAR. IEEE **40** (2004) 1147–1159.

[8] P. T. Gough, D. W. Hawkins: Imaging algorithms for a strip-map synthetic aperture sonar: Minimizing the effects of aperture errors and aperture undersampling. IEEE Journal of Oceanic Engineering **22** (1997) 27–39.

[9] N. Bleinstein: Physical optics farfield scattering in the time domain. J. Acoust. Soc. Am. **60** (1976) 1249–1255.

[10] N. Bleinstein: Direct image reconstruction of anomalies in a plane via physical optics farfield scattering. J. Acoust. Soc. Am. **59** (1976) 1259–1264.

[11] E. I. Thorsos: The validity of the Kirchhoff approximation for rough surface scattering using a Gaussian roughness spectrum. J. Acoust. Soc. Am. **83** (1988) 78–92.

[12] J. Ripoll, V. Ntziachristos, R. Carminati, M. Nieto-Vesperinas: Kirchhoff approximation for diffusive waves. Physical Revue E **64** (2001) 051917.

[13] A. J. Hunter, M. P. Hayes, P. T. Gough: Simulation of multiple-receiver broadband interferometric SAS imagery. Proc. OCEANS **5** (2003) 2629–2634.

[14] N. Bleinstein: Mathematical methods for wave phenomena. Computer Science and Applied Mathematics, Academic Press, 1984. 283.

[15] F. Schmitt, F. Daout: Wave scattering in underwater acoustics. J. Acoust. Soc. Am. **105** (1999) 1255.

[16] P. M.Morse, H. Fesbach: Methods of theoretical physics. Vol. 1. MacGraw-Hill, New York, 1953. Chapter 5, 623-624.

[17] N. Bleinstein: Mathematical methods for wave phenomena. Computer Science and Applied Mathematics, Academic Press, 1984. 82-89.

[18] N. Gespa: La diffusion acoustique par des cibles élastiques de forme géométrique simple, théorie et expériences. Imprimerie du CEDOCAR, 1987. Chap. 12(325).

[19] Y.-H. Pao, V. Varatharajulu: Huygens' principle, radiation conditions, and integral formulas for the scattering of elastic waves. J. Acoust. Soc. Am. **59** (1976) 1361–1371.

[20] F. Maussang, J. Chanussot, A. Hetet: Automated segmentation of SAS images using the mean. Standard deviation plane for the detection of underwater mines. Proc. OCEANS **4** (2003) 2155–2160.

[21] R. Van Vossen, J. Trampert, A. Curtis: Propagator and wave-equation inversion for near-receiver material properties. Geophysical Journal International **157** (2004) 796–812.